Research Square

Preprints are preliminary reports that have not undergone peer review.
They should not be considered conclusive, used to inform clinical practice,
or referenced by the media as validated information.

A Cross-Domain Orthogonal Spherical Interface for Bidirectional Haptic Human Robot Interaction

Wenbo Ding

ding.wenbo@sz.tsinghua.edu.cn

Tsinghua University https://orcid.org/0000-0002-0597-4512

Shoujie Li

Tsinghua University

Xingting Li

Tsinghua University

Chenxin Liang

Tsinghua University

Xie Xuanbing

Tsinghua University

Wei Hou

Tsinghua University

Zijian Lin

Tsinghua University

Chongxi Jiao

Tsinghua University

Mingshan He

Institute of Science Tokyo https://orcid.org/0000-0002-0369-5181

Junwei Li

Nanyang Technological University https://orcid.org/0000-0003-4493-3817

Jie Pan

Nanyang Technological University

Chuqiao Lyu

Tsinghua University

Xueqian Wang

Tsinghua University

Yifan Wang

Nanyang Technological University

Article

Keywords:

Posted Date: August 6th, 2026

DOI: https://doi.org/10.21203/rs.3.rs-10403008/v1

License: This work is licensed under a Creative Commons Attribution 4.0 International License.
Read Full License

Additional Declarations: There is **NO** Competing Interest.

Abstract

Integrating high-fidelity sensing and active feedback within a single flexible substrate remains a fundamental challenge in haptic interfaces due to the catastrophic signal crosstalk between co-located channels. This paper presents FusionTouch, a glove-free spherical haptic interface based on a cross-domain transparent architecture centered on optical accessibility, enabling multimodal sensing and haptic feedback on a flexible spherical skin. Leveraging a bio-inspired textile fabrication process, the skin seamlessly integrates a pneumatic support layer, a protective layer and a bidirectional layer composed of ITO, conductive hydrogel, and near-infrared markers, allowing electrical stimulation, optical sensing, photothermal modulation, and pneumatic support to work synergistically within the same interface while reducing interlayer imaging interference. Its spherical form factor is ergonomically inspired by the resting posture and manipulation movements of the human hand, conforming to the naturally curved and compact configuration of a relaxed hand, thereby improving ergonomic suitability for glove-free interaction. Powered by graph neural network and two-stream network algorithms, FusionTouch supports high-fidelity hand pose estimation (mean absolute error: 0.36°), three-dimensional surface deformation reconstruction (median error: 1.28 mm), and contact force estimation (mean absolute error: 0.093 N), while simultaneously providing localized electrotactile, photothermal, pneumatic stiffness, and optional vibrotactile feedback. Demonstrations in robotic teleoperation, virtual reality, and robot-assisted massage validate FusionTouch as a glove-free platform for bidirectional physical human–machine interaction and as a generalizable strategy for designing shared-surface interfaces that unify multimodal perception and haptic feedback.

One sentence summary

An ergonomic, glove-free spherical interface using cross-domain orthogonal pathways for crosstalk-reduced bidirectional haptics.

INTRODUCTION

Tactile interfaces provide the physical channel through which humans command robots, perceive remote contact, and interact with virtual environments (*1*). As robotic systems increasingly rely on human demonstrations to learn dexterous manipulation skills, and as immersive environments demand richer physical feedback, haptic human–machine interfaces are expected to perform two functions simultaneously: capturing hand motion and contact information with high fidelity, and rendering tactile cues such as contact, force, stiffness, and temperature in a programmable manner (*2, 3*). Achieving both functions in a single compact interface remains challenging because sensing and feedback elements are integrated on the same soft substrate, where electrical, optical, and mechanical interactions can degrade sensing accuracy, limit feedback richness, or reduce user comfort (*4, 5*).

Haptic gloves are the dominant solution for hand-based interaction and can capture finger motion using embedded sensor arrays (*6*). However, for long-duration use and bidirectional robot interaction, their

wearable form factor still presents several limitations. Dense electrical sensing increases wiring complexity and inter-channel coupling, creating trade-offs between spatial resolution and measurement robustness (*7, 8*). Many glove-based systems also provide only limited feedback modalities, most commonly vibration or proprioceptive force, whereas complex robot and virtual interactions require combinations of cutaneous, thermal, electrotactile,
and stiffness cues (*4, 9, 10*). In addition, enclosing the hand can constrain natural finger motion, require user-specific fitting, and induce fatigue during prolonged use (*11, 12*). Visuotactile sensors replace dense electrical sensing arrays with optical transduction, enabling high-resolution deformation sensing with reduced wiring complexity (*13–16*). However, most visuotactile systems are primarily used as dedicated sensors and do not provide rich haptic feedback. When feedback actuators are added to the same substrate, coupling between sensing and actuation channels may reappear. Therefore, a new interface architecture is needed to simultaneously achieve high-quality sensing, multimodal feedback, and comfortable hand interaction on a single soft interface while reducing task-relevant crosstalk among co-located functional channels.

Here we present FusionTouch, a glove-free spherical haptic interface based on a cross-domain architecture (Fig. 1A). FusionTouch integrates thermal, electrotactile, vibrotactile, and stiffness feedback with hand-gesture, contact-force, and surface-deformation sensing on a shared transparent soft spherical interface (Fig. 1B). Its design and validation are summarized in four aspects (movie S1). First, FusionTouch introduces a pneumatically supported spherical form factor inspired by hand-workspace statistics and relaxed-hand geometry, enabling glove-free hand support without enclosing the fingers (tables S1 and S2). Second, FusionTouch establishes an optical-accessibility-centered optical–electrical–pneumatic orthogonal architecture fabricated via a bio-inspired textile process. A spectral separation layer splits visible-light and near-infrared (NIR) optical pathways, forming distinct spectral channels within the shared transparent shell (Fig. 1C). In particular, the NIR channel supports both marker-based sensing and photothermal feedback, enabling perception and feedback to share the same spectral carrier (Fig. 1D). Patterned transparent indium tin oxide (ITO) electrodes introduce an electrical modality while preserving optical access (Fig. 1E), and pneumatic regulation adds an independent pressure-based modality for shell-level mechanical control (Fig. 1F). **Third**, FusionTouch develops a multimodal perception algorithm that fuses visible-light images, NIR marker observations, and pneumatic pressure through a two-stream network and a graph neural network. It achieves a surface-deformation reconstruction accuracy of 1.28 mm, a mean absolute contact-force error of 0.093 N, and 99.9% of selected joint-angle predictions within 5°. **Finally**, FusionTouch demonstrates improved contact-rich teleoperation and together with the proposed force-compliant operation framework, shows application potential in active–passive virtual reality, teleoperation, and robot-assisted massage scenarios (Fig. 1, G to J). Compared with representative human–machine and haptic interfaces (Fig. 1K and table S3) *(17–37)*, FusionTouch integrates broader sensing dimensions and feedback modalities within a transparent spherical platform, offering a new design paradigm for future human–machine interfaces.

RESULTS

Biomechanical rationale for a spherical interface

Although glove-based interfaces are widely used, they remain constrained by several inherent limitations, including interference with natural hand motion, susceptibility of electrical gesture-sensing components to failure or signal drift under frequent finger movements, and the need for hand-specific fitting, which limit their suitability for long-term and diverse human-machine interaction. To address this, we draw on a key biomechanical insight (supplementary text 1). Although the human hand possesses 21 degrees of freedom, it exhibits a well-defined rest posture in which both the intrinsic and extrinsic musculature are fully relaxed. The hand spontaneously assumes this configuration during sleep or anesthesia, corresponding to the state of greatest subjective comfort. Crucially, this posture is consistent across users without requiring individualized fitting.

To ground our design in quantitative biomechanics, we recruited 20 volunteers to analyze hand kinematics and workspace constraints. Motion-capture data in a relaxed state revealed that the palm and fingers spontaneously conformed to a near-spherical envelope (fig. S1). Furthermore, a systematic survey across 20 daily manipulation tasks (240,677 frames) showed that 99% of hand poses lie within a compact 15 cm spherical region (Fig. 1L and fig. S2). This natural congruence with hand kinematics supports an unconstrained workspace and directly motivates the spherical geometry *(38)* of FusionTouch.

To quantify this ergonomic advantage, the 8 volunteers rated the wearing comfort of FusionTouch and commercial data gloves (Manus Quantum Metagloves) across five dimensions: fit, pressure, flexibility, breathability, and long-term fatigue (Fig. 1M, fig. S3, and supplementary text 2). FusionTouch received a higher average comfort score of 84.82%, compared with 40.54% for the commercial gloves. This substantial gap demonstrates that aligning the spherical form factor with the hand's resting posture minimizes resistance to intrinsic muscle tension, thereby sustaining lower muscular load and higher comfort during use.

Cross-domain decoupled design of the spherical interface

Signal crosstalk and structural interference remain major challenges in multimodal haptic interfaces, particularly when sensing and feedback components are integrated on the same soft surface. FusionTouch addresses these challenges through an optical-accessibility-centered cross-domain orthogonal architecture, which distributes functions across spectral, electrical, and pneumatic domains. Here, optical accessibility means that visible and near-infrared (NIR) optical paths are prioritized in the structural layout, ensuring reliable access from the internal camera to the hand silhouette, elastomeric markers, and photothermal feedback regions. The term orthogonal does not imply complete physical

independence; rather, it denotes architectural separation among functional carriers, so that intermodal coupling is reduced at the design level before algorithmic compensation.

Concretely, visible light passes through the transparent conductive ITO film to the internal camera for hand-silhouette observation, whereas NIR illumination highlights infrared-opaque markers patterned on the same film for deformation and force sensing and is reused as a photothermal carrier for thermal feedback. The ITO layer provides an electrical pathway for electrotactile stimulation while preserving optical-path integrity, and pneumatic pressure independently modulates shell compliance. Thus, visible-light hand tracking, NIR marker-based deformation sensing, electrotactile stimulation, photothermal feedback, and pneumatic stiffness modulation are co-located on a single soft interface but rely on distinct physical carriers.

Because such orthogonality is approximate in practice, we identified and mitigated three representative residual coupling paths. Photothermal actuation induces temperature-dependent resistance changes in the ITO layer, but the resulting variation is much smaller than the skin-contact impedance and remains within the compensation range of the current-regulated electrotactile driver. NIR illumination fluctuations can alter raw-image grayscale values; this effect is mitigated by converting detected markers into geometric graph representations based on position, area, shape, and topology, making deformation reconstruction and force estimation insensitive to global illumination intensity. Pneumatic stiffness modulation changes the deformation–force relationship of the shell, which is compensated by incorporating real-time internal pressure as a conditioning input to the force-perception network.

Interference tests under five feedback conditions—no feedback, thermal, electrotactile, pneumatic, and vibrotactile—confirmed the effectiveness of these mitigations. Marker-detection accuracy remained around 96% across conditions, with a maximum change of 0.96 percentage points relative to the no-feedback baseline (table S4); gesture-estimation accuracy remained around 98%, with a maximum change of 0.45 percentage points. Thermal feedback increased the electrode-path resistance from 1.302 to 1.387 kΩ, a minimal change of 0.085 kΩ that was negligiblecompared with the typical dry-electrode skin-contact impedance of 10–100 kΩ (39) and remained within the compensation range of the current-limited driver. Together, these results indicate that FusionTouch achieves task-level functional decoupling among optical sensing, thermal feedback, electrotactile stimulation, and pneumatic stiffness modulation on a shared spherical interface, without requiring dense co-located electrical sensor arrays.

Modular spherical fabrication and performance characterization

FusionTouch consists of two main components: an imaging system and a spherical flexible skin. The imaging system integrates near-infrared cameras, visible-light cameras, and high-power near-infrared LEDs, where the high-power infrared LEDs provide illumination and enable thermal feedback. The skin adopts a three-layer stacked architecture, including a thermoplastic rubber (TPR) support layer that

provides elasticity and pneumatic stiffness modulation, a bidirectional layer that integrates ITO, conductive hydrogel, and near-infrared markers, and an easily replaceable fabric-based protective layer. This fabric protective layer improves hygiene and helps prevent cross-contamination (Fig. 2, A and B). A long-standing challenge in spherical flexible skins is that mature textile and lithographic processes are typically based on planar substrates and therefore cannot directly fabricate a closed spherical surface. Inspired by the natural geometries of physalis fruit, mangosteen, citrus segments, and paper lanterns, we developed a fan-sector textile process that conformally maps the three-dimensional spherical surface into a set of planar petal-shaped segments (Fig. 2C). Each segment is fabricated using a programmable computer-controlled sewing machine: the fabric, ITO film, and non-woven reinforcement layer are clamped in upper and lower frames; the sewing paths are pre-programmed to define the electrode geometry; infrared-opaque ink is then used to print the markers, followed by drying (Fig. 2D and fig. S4). Finally, the segments are assembled into a closed sphere through edge bonding, forming the spherical FusionTouch interface. This modular architecture reduces tooling cost, supports individual replacement of damaged segments, facilitates replacement of the outer fabric layer, and remains compatible with conventional textile manufacturing infrastructure.

To understand the mechanical role of the protective outer layer, we conducted finite element method (FEM) simulations comparing systems with and without this layer (supplementary text 3 and fig. S5). The numerical results reveal that the outer layer effectively confines the pressurized inflation of the inner TPR shell, significantly enhancing the overall contact stiffness under identical indentation and pressure conditions. We further characterized the mechanical, electrical, optical, and thermal responses of FusionTouch (Fig. 2, E to J). For mechanical characterization, the spherical interface was indented along the Z axis under five internal pressures of 5, 25, 50, 75, and 100 mbar, and the relationship between Z-axis displacement and normal contact force was recorded (Fig. 2E). The force–displacement curves exhibited nonlinear responses, indicating that the mechanical response of FusionTouch cannot be described by a simple linear spring model but depends jointly on indentation depth and internal pressure. At an indentation depth close to 30 mm, the normal forces were approximately 2.48, 9.75, 15.81, 23.55, and 29.23 N, respectively. Thus, increasing the internal pressure substantially increased the contact force at the same indentation depth, demonstrating that the apparent stiffness of FusionTouch can be continuously tuned by pneumatic control.

Characterization of the electrotactile driving circuit further confirmed its programmable stimulation capability. By changing the resistance setting in the circuit, the maximum output voltage increased from 55.53 V at 1000 Ω to 94.00 V at 400 Ω (Fig. 2F). While maintaining high-voltage pulse output, increasing the duty cycle from 1% to 50% expanded the effective pulse width from approximately 0.015 to 1.24 ms (Fig. 2G). In addition, the current-control module enabled milliampere-level regulation of stimulation intensity, with an output current up to approximately 4.37 mA (Fig. 2H). These results show that FusionTouch can independently regulate voltage amplitude, pulse width, and current intensity, thereby supporting programmable electrotactile feedback.

We also evaluated the spectral selectivity of the infrared absorbing dye layer (Fig. 2I and fig. S6). As the dye concentration increased from 0 to 1.5%, the transmittance in the infrared channel decreased continuously from 93.4% to 12.3%, whereas the visible-light transmittance remained above 72.9%. Although the ultraviolet transmittance also decreased, it remained substantially higher than the infrared transmittance at high dye concentrations. This selective attenuation allows the infrared markers to form distinct features under infrared illumination while preserving visible-light observation of the hand. Finally, in open-loop bench tests without skin contact, infrared-LED heating experiments showed that the surface temperature could be modulated from approximately 44.97 °C to 88.20 °C by adjusting the driving voltage from 10 to 22 V (Fig. 2J); during human interaction, a closed-loop thermistor controller caps the contact temperature below 48 °C (40). Together, these results demonstrate that FusionTouch integrates tunable stiffness, programmable electrotactile stimulation, optical selectivity, and broad-range photothermal feedback within a single spherical interface.

Multimodal sensing performance

A closed-loop haptic interface demands co-located perception of contact location, interaction strength, and user intent within a single, unified device. We therefore rigorously characterized the stability and fidelity of these functional sensing signals provided by the spherical multimodal interface of FusionTouch. Leveraging this spectrally separated optical design, FusionTouch simultaneously captures visible-light and near-infrared information (Fig. 3, A to C) during a single contact event, from which different modal features can be extracted. First, surface-deformation reconstruction maps the precise contact geometry on the soft shell, establishing the spatial foundation required for localized electrotactile feedback. Second, contact-force estimation quantifies the mechanical loading applied to the interface, supplying the essential intensity signal for dynamic feedback modulation and compliant force control. Finally, hand-posture estimation captures the wearer's kinematic intention without the need for a restrictive glove, enabling FusionTouch to function as an intuitive input device for robotic and virtual interactions. Together, these three sensory outputs bridge the spherical interface to localized stimulation, force-aware control, and user-command generation in the subsequent demonstrations.

Surface deformation reconstruction. We first evaluated the three-dimensional surface reconstruction performance of FusionTouch under controlled contact deformation. This task aims to recover the deformed geometry of the spherical skin, providing the spatial basis for interpreting contact location and contact-induced deformation. In FusionTouch, deformation is inferred from the marker field patterned on the inner surface of the shell. Under internal illumination, the markers form a detectable pattern, and their spatial layout and displacement provide the geometric cues used for reconstruction (Fig. 3D and supplementary text 4). The reconstruction dataset was constructed from 13 controlled pressing geometries (fig. S7). For each contact geometry, we applied contact at 36 angular positions across the spherical sensing region, thereby generating paired marker observations and ground-truth point-cloud labels spanning diverse contact locations and deformation patterns. We propose a two-stage coarse to fine graph network for 3D reconstruction. The algorithm is illustrated in Fig. 3E and further explained in

supplementary text 5. In total, the dataset contains 468 deformation configurations across the 150 mm-diameter sensing region. We compared the reconstructed point clouds with ground-truth point clouds on a held-out test set of 52 contact configurations. FusionTouch achieved a Chamfer-distance RMSE of 1.77 ± 0.34 mm, corresponding to 1.18% of the sensor diameter, with a median point-to-surface error of 1.28 ± 0.04 mm and a point-cloud precision of 0.875 ± 0.043 (Fig. 3, F and G). The errors were concentrated near the mean, with a small number of boundary cases forming the long tail. These results (fig. S8, fig. S9, fig. S10, fig. S11, table S5 and movie S2) show that FusionTouch reconstructs contact-induced spherical deformation at millimeter scale, providing a dense geometric signal for contact analysis.

Contact force estimation. We then evaluated whether FusionTouch can estimate the three-axis force applied to the same soft interface. Because the mechanical response of the inflated shell depends on its pneumatic state, the same marker displacement may correspond to different forces under different internal pressures. We therefore fuse the near-infrared marker image with the internal pressure measurement for force estimation. Specifically, we introduce a dual-branch graph-based network, where one branch processes the marker graph directly and the other branch encodes the pressure information into patched near-infrared images before feature extraction. The two feature streams are then fused to estimate the three-axis contact force (Fig. 3H and supplementary text 6). The model was trained and evaluated on 96,000 force measurements spanning 0–30 N across four pressure levels of 5, 15, 25, and 35 mbar (Fig. 3, I and J). On the held-out test set, FusionTouch achieved an overall MAE of 0.093 N and an RMSE of 0.172 N. The per-axis MAE was 0.043, 0.043, and 0.193 N along Fx, Fy, and Fz, respectively, with the larger Fz error reflecting the broader dynamic range of the normal force. Removing pressure conditioning increased the overall MAE from 0.093 to 0.161 N and the RMSE from 0.172 to 0.303 N; the Fz error increased from 0.193 to 0.328 N (Fig. 3L). This comparison confirms that the pneumatic state provides essential information for disambiguating force from deformation (fig. S12, fig. S13 and table S6). Overall, FusionTouch estimates three-axis contact force with an overall MAE of approximately 0.1 N, providing the force feedback signal required for closed-loop teleoperation and physical interaction.

Hand pose estimation. In addition to contact geometry and force, FusionTouch can infer the wearer's hand posture to serve as a natural input device. This experiment evaluates whether the spherical interface can capture user motion without requiring a glove. FusionTouch uses the visible-light image to capture the hand silhouette on the spherical surface and the near-infrared image to capture the marker deformation induced by hand contact. A two-branch ResNet-18 network encodes the two images separately and fuses their latent features to regress a 12-dimensional selected finger-joint representation (Fig. 4B and supplementary text 7). Although the data glove provides 17 joint-angle channels, we use 12 selected channels, including $r0$, $r1$, $r2$, $r4$, $r5$, $r7$, $r8$, $r9$, $r12$, $r13$, $r16$, and $r17$. We use this reduced representation because interaction with the spherical interface is dominated by finger motion, whereas the palm remains approximately supported by the device surface and exhibits relatively limited motion during operation. The selected joints therefore capture the main posture variations used for gesture input and teleoperation control without introducing weakly varying palm-

related degrees of freedom. On a held-out test set of 2,179 frames, the dual-modality model achieved an overall MAE of 0.36° and an RMSE of 0.60° across the 12 joints, with 92.4% of predicted joint angles within 1°, 98.5% within 2° and 99.9% within 5° of the ground truth. Single-modality inputs were consistently less accurate, with the near-infrared-only model reaching 0.45° MAE and the visible-light-only model reaching 0.57° MAE. Dual-modality fusion reduced the MAE by 21% relative to the better single modality and decreased the 95th-percentile error from 1.57° to 1.22° (Fig. 4C). These results (fig. S14, fig. S15 and table S7) show that visible hand appearance and contact-induced marker deformation provide complementary cues, enabling FusionTouch to recover glove-free hand posture with sub-degree accuracy.

Robotic teleoperation across platforms and end-effectors

Robotic teleoperation is increasingly important for embodied-AI data collection and remote manipulation, but current systems remain limited by two practical constraints. First, different end-effectors often require dedicated control interfaces, making it difficult to use a single natural input device across platforms. Second, contact information at the remote end is usually weakly conveyed to the operator, and existing haptic feedback is often limited to point-wise or global cues. FusionTouch addresses these limitations by integrating hand-pose input, end-effector retargeting, and spatially localized electrotactile feedback within one spherical interface, allowing operators to control different robotic platforms while perceiving remote contact location and intensity. We evaluated FusionTouch as a robotic teleoperation interface that couples arm-level motion control, hand-pose retargeting, and closed-loop tactile feedback (Fig. 4). The system supports two control modes (Fig. 4A). In the handheld mode, an Intel T265 tracker measures the relative pose of the handheld FusionTouch device, and the pose increment is mapped to the end-effector motion of a UR5 arm. In the master–slave mode, joint angles from a Songling Piper master arm are mapped directly to the slave arm. Both modes use the same FusionTouch-based hand-pose input and tactile-feedback pathway, allowing the interface to be coupled to distinct robot platforms and control architectures

End-effector control was driven by a bimodal hand-pose estimation network (Fig. 4B). RGB images capture the hand configuration on the spherical interface, whereas infrared images capture marker deformation and topology on the shell. Each stream is encoded by a ResNet-18 backbone into a 512-dimensional feature vector, and the fused representation is regressed to hand-joint states for retargeting to either an X-Hand dexterous hand or a gripper. Compared with RGB-only or infrared-only inputs, bimodal fusion shifted the cumulative error distribution toward lower per-sample angular error (Fig. 4C), supporting more reliable teleoperation commands. We then tested two classes of teleoperation tasks (Fig. 4D). The first class comprised manipulation tasks with clear task constraints, including hanging a cup, scooping rice, folding a towel, and opening a drawer (movie S3 and S4). The second class comprised grasp-and-place trials over daily objects and foods (movie S5).. Daily-1 denotes relatively large elongated objects, Daily-2 denotes smaller objects that are difficult to grasp, Food-1 denotes large rounded foods, Food-2 denotes small fragile foods, and Food-3 denotes elongated foods.

Tactile feedback was associated with shorter completion times and higher first-attempt success rates. Four participants completed the teleoperation evaluation in a within-subject design. For the grasp-and-place success-rate analysis, each participant performed five trials for each object category under each feedback condition, yielding 20 trials per object category per condition and 200 grasp-and-place trials in total. The feedback order was counterbalanced across participants, and the object-category order was varied across participants to reduce order effects. With feedback, the mean completion times for cup hanging, rice scooping, towel folding, and drawer opening decreased from 20, 33, 24, and 12 s to 12, 28, 11, and 7 s, corresponding to reductions of approximately 8, 5, 13, and 5 s (Fig. 4E and table S8). The first-attempt success rates for Daily-1, Daily-2, Food-1, Food-2, and Food-3 increased from 85%, 75%, 80%, 60%, and 80% to 95%, 90%, 85%, 80%, and 90%, respectively (Fig. 4F and table S9). Across all object categories, the pooled first-attempt success rate increased from 76/100 trials (76%) without tactile feedback to 88/100 trials (88%) with tactile feedback. An exploratory two-sided two-proportion test on the pooled trial counts indicated an overall improvement with tactile feedback (p = 0.027). The lower no-feedback success rate for Food-2 reflects the greater difficulty of small, fragile foods, which require precise low-force grasping and are more prone to slipping or deformation.

Closed-loop feedback was implemented by mapping fingertip pressure measured at the robot end-effector to electrotactile stimulation intensity on the corresponding region of the FusionTouch surface. Because the operator's finger placement on the spherical interface is stable after calibration, contact at a given robotic fingertip can be rendered as localized stimulation at the homologous operator-side region, with stronger remote pressure producing stronger electrotactile feedback. This region-selective feedback was used across simple gripper grasping, X-Hand dexterous grasping, and X-Hand in-hand manipulation demonstrations (Fig. 4, G to I), providing contact cues for different end-effectors without changing the handheld interface.

Active and passive VR interaction

Virtual-reality interaction has long relied on visual rendering and hand tracking, but visual cues alone cannot provide the physical sensation of object motion, collision response, or contact forces during physical interaction with virtual objects. FusionTouch extends VR interaction by combining cutaneous feedback, robot-mediated displacement, and force control. Thus, virtual contact can be rendered through electrotactile and thermal cues, end-effector motion, and controlled contact forces. By integrating passive dragging and active robot motion in one system, FusionTouch links the VR scene, robotic actuation, and human tactile perception through a unified interface. We built a FusionTouch-driven VR–robot haptic interaction system. The system supports passive and active modes (Fig. 5A). Object calibration and hand calibration establish the transformation between the VR tracking space and the robot end-effector, and force control is used to preserve compliant and safe contact during interaction.

In passive mode, the robot is placed in a gravity-compensated drag state (movie S6). The operator directly pushes or pulls the arm, while FusionTouch measures contact force and the controller estimates

the kinematic state of the end-effector. When the external force is removed, the end-effector velocity is damped to zero and the current pose is maintained. This mode is suited to interactions that require direct human intervention and physical compliance. Fig. 5B shows two representative tasks: virtual apple harvesting and steamed-bun pickup. Both tasks use electrotactile feedback to render contact state. In the steamed-bun task, the infrared lamps additionally provide illumination and heating. Under infrared illumination, the markers on the shell appear as opaque features for internal deformation reconstruction; under visible light, the markers remain transparent and do not obstruct hand observation. The same infrared illumination provides photothermal heating, allowing the interface to render warmth during contact with the virtual hot object.

In active mode, the end-effector trajectory can be generated from either a predefined target path or hand tracking (movie S7). In the first case, the robot executes a prescribed trajectory and applies a programmed response after contact; in the volleyball task, the target approaches the hand and rapidly rebounds after contact, mimicking the reaction of a struck ball. In the second case, Meta Quest 3 measures the operator's hand position in the VR space, and the transformed pose is used to generate the end-effector target; in the animal-stroking task, the end-effector follows the hand within the valid workspace, pauses when the hand leaves the trackable range, and resumes when the hand re-enters it. Both trajectory sources are executed through force control, allowing the robot to follow the target motion while maintaining compliant contact and reducing impact during interaction (Fig. 5C).

FusionTouch encodes both the contact region and contact intensity during these interactions. As the hand transitions from light touch to gentle squeeze, moderate squeeze, and firm squeeze, the activated area on the spherical interface expands and the electrotactile current increases (Fig. 5D and fig. S16). The corresponding hand maps show progressively stronger and broader feedback distributions, demonstrating that the same interface can convey not only contact occurrence but also where contact occurs and how strongly it is applied.

Robot-assisted back massage

Robot-assisted massage and rehabilitation can deliver repeatable, quantifiable physical therapy through controlled mechanical stimulation of soft tissues, helping to relieve muscle tension, promote local circulation, and improve tissue compliance *(41, 42)*. However, manual massage suffers from inherent variability in contact force, rhythm, and spatial coverage, making therapeutic outcomes difficult to standardize or reproduce; moreover, controlled mechanical stimulation has been shown to promote functional recovery of injured skeletal muscle and modulate local inflammatory responses *(43)*, suggesting that precise force delivery may yield physiological benefits unattainable through inconsistent manual contact. Robotic systems offer a principled path toward such controllable and repeatable stimulation.

Achieving this goal requires an end-effector that can maintain compliant contact, regulate contact force, and provide perceptible feedback during continuous human contact. Conventional systems typically rely

on external force sensors and separate stimulation modules, increasing hardware complexity. FusionTouch offers an integrated alternative: the spherical interface senses contact force from its own deformation and internal pressure, delivers thermal and electrotactile feedback, and modulates stiffness through pneumatic regulation. We therefore mounted FusionTouch on a UR5 robotic arm to construct a robot-assisted back-massage system (fig. S17), in which FusionTouch simultaneously served as the compliant massage end-effector, force-sensing unit, heating module, and electrotactile stimulation interface. This integration enables force-controlled massage without an additional six-axis force/torque sensor while supporting compliance tuning and multimodal feedback for massage and rehabilitation scenarios.

The controller combines XY-plane position control with Z-axis admittance control (Fig. 5E). In the XY plane, the controller computes planar velocity commands from the target and current end-effector positions to cover the massage region. Along the Z axis, the controller computes a vertical velocity command from the force error: the end-effector moves downward when the contact force is below the target and retracts when the force is excessive. The two velocity commands are fused and sent to the robot hardware, enabling compliant motion over the curved back surface.

The force and displacement traces show two representative massage modes (Fig. 5F). During continuous massage, the contact force was maintained near 5 N while the interface slid over the back. During tapping, the controller generated periodic force peaks of approximately 10 N and released contact after each press. The relative Z displacement adapts to changes in surface height, indicating that the controller can accommodate non-planar body curvature while maintaining stable pressure.

Mechanical force control was augmented by infrared heating and electrotactile stimulation. Heating provides warmth, whereas electrotactile pulses with different frequencies and amplitudes provide graded cutaneous stimulation (movies S8). Low-intensity stimulation can enhance the sensation of sustained contact and sliding, whereas stronger stimulation can be paired with deeper pressing or tapping to produce a more pronounced massage sensation. By integrating force-controlled contact, thermal feedback, electrotactile stimulation, and a soft self-sensing end-effector in one device, FusionTouch provides a compact platform for robot-assisted massage and rehabilitation-oriented human-robot interaction.

DISCUSSION

Tactile human–machine interfaces are moving from unidirectional sensing or feedback devices toward bidirectional physical communication platforms that can simultaneously capture human intent and render contact information. FusionTouch contributes to this direction by introducing a glove-free spherical interface that integrates hand-pose sensing, surface-deformation perception, contact-force estimation, and multimodal haptic feedback on a shared soft surface. Unlike glove-based interfaces that enclose the hand, FusionTouch derives its form factor from the natural geometry of hand motion. The biomechanical results show that most daily hand postures are contained within a compact spherical

workspace and that the relaxed hand naturally adopts a curled configuration. This correspondence between hand kinematics and spherical geometry provides a physical basis for replacing the glove with a soft spherical interface, thereby reducing finger constraint, avoiding hand-specific fitting, and improving comfort during prolonged interaction.

A second contribution of FusionTouch is its optical-accessibility-centered cross-domain integration strategy, facilitated by a bio-inspired textile process that simplifies fabrication. Instead of stacking multiple sensing and actuation components within a single electrical or mechanical layer, FusionTouch distributes diverse functionalities across distinct physical domains while maintaining optical accessibility: visible light is utilized for hand observation, near-infrared (NIR) light for marker-based deformation sensing and photothermal feedback, transparent indium tin oxide (ITO) electrodes for electrotactile stimulation, and pneumatic pressure for stiffness modulation. This co-design, realized via the straightforward, textile-based integration of heterogeneous materials, enables multimodal sensing and feedback to coexist on a single compliant spherical surface without compromising optical access to the hand or mechanical compliance. Consequently, FusionTouch can simultaneously support hand tracking, surface-deformation perception, contact force estimation, and multi-modal haptic rendering in a compact, glove-free form factor.

The experimental results demonstrate that this architecture enables a combination of sensing and feedback capabilities that are difficult to achieve in conventional wearable or tactile-sensor-based systems. FusionTouch achieves millimeter-scale surface-deformation reconstruction, accurate hand-pose estimation, and approximately 0.1-N contact-force estimation, while also providing co-located electrotactile, thermal, stiffness, and vibrotactile feedback. These capabilities allow the same physical interface to be used across robotic teleoperation, virtual reality, and robot-assisted massage. In teleoperation, FusionTouch provides hand-motion input and contact-related feedback for robotic manipulation. In virtual reality, it maps hand interaction and surface contact to multimodal haptic rendering. In robot-assisted massage, the compliant spherical body functions not only as an interaction interface but also as a self-sensing contact medium. These demonstrations suggest that a shared-surface, cross-domain haptic interface can serve as a general platform for bidirectional physical human-machine interaction, rather than as a task-specific sensor or actuator.

Although FusionTouch's cross-domain architecture reduces direct inter-modal interference, residual coupling remains in a compact compliant interface, including thermal effects on ITO resistance, illumination-dependent changes in marker visibility, pressure-induced changes in shell mechanics, and vibration-induced motion artifacts. The current system mitigates these effects through current-regulated driving, wavelength-separated imaging, geometric marker-based reconstruction, and pressure-conditioned force estimation, maintaining stable marker detection, gesture estimation, and electrotactile output within the evaluated operating range.

Future work should further quantify crosstalk, long-term drift, and mechanical fatigue under all-on multimodal operation, while addressing the lack of active cooling, the limited spatial resolution of

thermal and vibrotactile feedback, the absence of localized stiffness modulation, and the continued reliance on external pneumatic and electronic connections. Subsequent efforts will focus on active cooling, localized stiffness modulation, high-resolution haptic feedback, and wireless self-contained integration, together with larger-scale user studies and direct comparisons with commercial devices to evaluate task performance, learning effects, long-term comfort, and inter-user variability.

MATERIALS AND METHODS

Hand-workspace study

In the hand-workspace study, 20 participants wore Manus Quantum Metagloves high-precision data gloves and performed 20 common manipulation tasks (table S10), spanning representative scenarios such as paper cutting, towel folding, battery installation, and USB insertion. The gloves operate on an electromagnetic field (EMF) tracking principle and support 25-degree-of-freedom hand joint motion capture. It should be noted that the gloves provide kinematic information only and do not offer any form of tactile feedback. Throughout the experiment, the gloves continuously recorded hand-joint kinematics of the dominant hand, from which the three-dimensional positions of multiple finger skeletal nodes, including MCP and distal finger nodes, were obtained for each frame, yielding 240,677 frames of data for subsequent processing and analysis.

Based on these recordings, we quantified the natural hand-operation workspace through the following pipeline. First, the mean position of the metacarpophalangeal (MCP) joint nodes of each finger was taken as the palm-root reference origin, and the distal joint nodes from the proximal segment to the fingertip of each finger (4 nodes per finger, 20 in total) were extracted as the hand-pose descriptor for each frame. Second, for each finger, an algebraic sphere equation was fitted to the four nodes via least-squares regression to obtain a ”curvature sphere,” whose radius encodes the degree of finger flexion — a smaller radius indicates greater curvature. When the four nodes were approximately coplanar and the fit degenerated, the method fell back to computing the minimum enclosing sphere of those nodes, with an upper-bound radius check applied to reject outlier solutions. The finger exhibiting the highest curvature was then selected as the representative finger for that frame. Subsequently, the proximal MCP node of each finger was excluded to prevent the enclosing sphere from being artificially enlarged by an open palm; the Welzl algorithm was then applied to the remaining 15 distal nodes to compute the minimum enclosing sphere — the unique sphere of smallest radius (fig. S18) whose center lies within the convex hull of those nodes — representing the minimal spherical workspace required to encompass all finger nodes in that frame (fig. S19). Statistical analysis across all collected frames was used to assess whether a spherical interface can effectively cover the full range of typical hand motions.

In a separate experiment, we collected the resting-posture configurations of 20 volunteers’ hands, defined as the natural hand shape adopted when both intrinsic and extrinsic muscles are fully relaxed. To ensure a truly unconstrained relaxed state, an external RGB-D camera was used to capture a monocular RGB frame of each volunteer’s hand, and the HaMeR (35) algorithm was applied to estimate the hand

mesh and three-dimensional hand keypoints from the RGB image, thereby characterizing the resting posture without imposing any external constraints (fig. S20). The results demonstrate that, when fully relaxed, the five fingertips naturally converge and conform to an approximately spherical envelope surface, directly validating the rationale behind FusionTouch's spherical geometric design.

Data collection

We collected three datasets to support the training of FusionTouch's multimodal perception models: a teleoperation mapping dataset, a three-dimensional surface reconstruction dataset, and a force-calibration dataset.

For teleoperation mapping, participants wore a commercial data glove and performed representative hand gestures on the FusionTouch surface to cover the hand poses expected during teleoperation (supplementary text 8 and fig. S21). The data glove provided joint-angle vectors, while the internal RGB and infrared cameras of FusionTouch simultaneously recorded visible-light images and infrared marker images. Each sample consisted of an visible-light image, an infrared image, and the corresponding joint-angle label. In total, nearly 22,000 paired samples were collected for training the hand-pose mapping model.

For three-dimensional surface reconstruction, we fabricated 13 molds with known geometries. For each mold, the inner-surface geometry was extracted algorithmically from the corresponding OBJ model and represented as a point cloud, which served as the ground-truth geometric label. During collection, each printed mold was placed over the outer surface of FusionTouch to impose a known deformation on the spherical shell, while the internal infrared camera recorded the corresponding marker image. Each mold was rotated through 360 degrees in 10-degree increments, yielding 36 views per mold (fig. S22). The resulting dataset therefore paired infrared marker images with point-cloud labels across 13 mold geometries and 36 orientations per geometry.

For force calibration, FusionTouch was rigidly connected to a high-precision six-axis force/torque sensor, and the assembly was mounted at the end of a UR robotic arm (fig. S23). The force/torque sensor recorded three-axis force and three-axis torque at 1 kHz. Before each experiment, the unloaded sensor output was measured to estimate the bias, which was subtracted during data acquisition. Data were collected under four pneumatic pressure settings of 5, 15, 25, and 35 mbar, and the same robotic pressing protocol was repeated for each parameterized pressing panel under each pressure condition to isolate the effect of pneumatic state.

In each force-calibration trial, the robot first moved to a vertical downward initial pose and slowly advanced along the Z-axis until contact was detected. Contact onset was defined when the Z-axis force exceeded 0.05 N. The robot then scanned along the Y direction over a 12-cm range with a 5-mm step size. At each Y position, the robot pressed an additional 4 cm along the Z axis with a 0.5-mm step size. At each sampling point, the two internal camera images, six-axis force/torque reading, pneumatic

pressure, and robot TCP pose were recorded synchronously. Each parameterized panel generated approximately 2000 samples under a single pressure condition. Across approximately 12 panels (fig. S24) and four pressure conditions, we collected approximately 96,000 force-calibration samples for training the contact-force perception model.

Size and system design

The hardware and software architecture of FusionTouch is organized into distinct functional modules coordinated by a centralized host computer, spanning an internal vision module, a pneumatic regulation module, a thermal feedback module, an electrotactile feedback module, and an application-level control module. Mechanically, FusionTouch is designed to operate as a spherical interface with an approximate diameter of 15 cm under nominal inflation (fig. S25). This co-located hardware-software framework enables synchronized multi-sensory data acquisition and precise haptic rendering.

The internal vision module contains one visible-light camera and one near-infrared camera, both connected to the host computer through USB. The visible-light image captures the hand contact posture on the spherical interface, whereas the near-infrared image captures the deformation and topology of the surface markers. The host computer timestamps both image streams and transfers them through queues to the neural-network inference and control threads, providing a unified internal observation for hand-pose estimation, surface reconstruction, and contact-force estimation. The pneumatic regulation module consists of two high-flow air pumps and a proportional valve, which control the inflation state and mechanical compliance of the spherical body. The proportional valve communicates with the host computer through RS485 and uses its built-in pressure sensor for closed-loop pressure regulation. During experiments and interaction tasks, the system typically operated at an internal gauge pressure of 5 to 50 mbar. The pressure reading was recorded synchronously and used as one input for force estimation and tactile perception models.

The thermal feedback module utilizes internal infrared LEDs driven by an independent adjustable power supply, where the heating intensity is regulated by changing the driving voltage or input power. A temperature sensor placed near the infrared heating elements monitors the local temperature. When the measured temperature is abnormal or exceeds the preset range, the host computer reduces the infrared LED output. The same infrared channel is therefore used for marker illumination and photothermal feedback.

The electrotactile feedback module is driven by a fabric electrode array and embedded driving circuits. The electrode layer consists of four petal-shaped modules, each containing 14 electrode sites, yielding 56 electrode sites in total. Each petal is controlled by an embedded controller board. The host computer sends the stimulation pattern, target channel, and intensity parameters to the controller through USB (fig. S26). The controller adjusts the stimulation intensity through a DAC, operational amplifier, and current-control circuit, and routes the output to selected electrodes through a high-voltage multiplexer (fig. S27).

Although the channels are scanned serially at the circuit level, the refresh rate is sufficiently high to produce a perceptually near-synchronous regional tactile sensation.

At the application level, the control module integrates FusionTouch sensing, robot control, and virtual-environment information. In teleoperation, internal images from FusionTouch are processed by the hand-pose estimation network to obtain finger-joint states, which are then mapped to control commands for a dexterous hand or gripper; arm motion is provided by either T265 pose input or a master–slave control link. In VR interaction, Meta Quest and Unity provide hand displacement, virtual-object states, and contact events, which are transferred through the host computer to the robot and FusionTouch. The virtual objects in Unity are updated according to FusionTouch motion and contact feedback, whereas contact events are mapped to electrotactile, thermal, or mechanical feedback. In robot-assisted massage, FusionTouch is mounted at the robot end effector through the bottom mechanical interface and functions as a soft massage head, force-sensing unit, and multimodal feedback module; the robot follows a prescribed trajectory while adjusting its normal response according to the contact force estimated by FusionTouch.

Safety monitoring and protection

To mitigate safety risks during feedback, FusionTouch integrates internal temperature and pressure sensors along with a current-monitoring circuit, enabling real-time supervision of thermal, pneumatic, and electrotactile outputs. Specifically, the temperature sensor monitors surface heating during photothermal feedback to prevent overheating, the pressure sensor tracks the internal pressure of the spherical shell to avoid over-inflation or operating outside the designed compliance range, and the current-monitoring circuit continuously measures the stimulation current to prevent overcurrent exposure. System protection focuses heavily on electrotactile output and robotic motion safety: the electrotactile driving circuit combines hardware current limiting and software constraints to keep the stimulation current below approximately 4.5 mA, while the power-management circuit includes transient-voltage suppression to reduce the impact of high-voltage pulses and supply disturbances; on the robot side, workspace limits, controller safety boundaries, and emergency-stop functions prevent the end effector from moving beyond the operating range or generating abnormal motion.

When abnormal heating, overpressure, or excessive stimulation current is detected, the controller automatically limits or interrupts the corresponding feedback channel. Specifically, photothermal heating is reduced or turned off when the measured temperature approaches the upper limit, pneumatic actuation is stopped or vented when the internal pressure exceeds the allowable range, and electrotactile stimulation is disabled when the detected current exceeds the preset threshold. Together, these hardware and software safeguards constrain the thermal, pneumatic, and electrical outputs within predefined operating limits, thereby reducing the risk of user discomfort or injury during operation.

Declarations

Acknowledgments

Funding:

This work was supported by the National Key R&D Program of China (grant no. 2024YFB3816000 to W.D.), the Shenzhen Science and Technology Program (grant no. KJZD20240903100905008 to W.D.), the Guangdong Innovative and Entrepreneurial Research Team Program (grant no. 2021ZT09L197 to W.D.), and the Singapore Ministry of Education (MOE) Tier-1 Award (grant no. RG146/24 to Y.W.).

Ethics approval:

Ethical approval was obtained from the Ethics Committee of Tsinghua Shenzhen International Graduate School, with Ethics Approval No. ETH-F2026083.

Author contributions:

W.D., Y.F.W., and S.L. conceived the idea, supervised and administered the project, and secured funding and resources. S.L., X.T.L., C.X.L., C.X.J., and M.S.H. developed the methodology. C.X.L. developed the software. S.L., X.T.L., C.X.L., C.X.J., X.X., W.H., and Z.L. performed the formal analysis. S.L., X.T.L., X.X., W.H., and Z.L. conducted the investigation. S.L., X.T.L., and C.X.L. drafted the manuscript. W.D., Y.F.W., S.L., C.X.L., C.X.J., X.X., W.H., Z.L., J.W.L., J.P., C.Q.L., and X.Q.W. revised and edited the manuscript. All authors discussed the results and commented on the manuscript.

Competing interests:

There are no competing interests to declare.

Data and materials availability:

The main text and the Supplementary Materials include the data supporting this study's findings. Codes used for training models and weights are available at https://github.com/RavenLiang1005/FusionTouch-Offical-Code.git. The data that support this study are available at https://drive.google.com/drive/folders/18F-MSTW4Jsv_V3Wuul25g-B7k6M6c4tm? usp=drive_link.

References

1. X. Yu, *et al.*, Skin-integrated wireless haptic interfaces for virtual and augmented reality. *Nature* **575** (7783), 473–479 (2019).
2. S. An, *et al.*, Dexterous manipulation through imitation learning: a survey. *IEEE Transactions on Automation Science and Engineering* **23**, 1760–1792 (2026).
3. B. Spittle, M. Frutos-Pascual, C. Creed, I. Williams, A review of interaction techniques for immersive environments. *IEEE Transactions on Visualization and Computer Graphics* **29** (9), 3900–3921 (2022).

4. S. Patel, Z. Rao, M. Yang, C. Yu, Wearable haptic feedback interfaces for augmenting human touch. *Advanced Functional Materials* **36** (6), 2417906 (2026).
5. M. van Wegen, *et al.*, An overview of wearable haptic technologies and their performance in virtual object exploration. *Sensors* **23** (3), 1563 (2023).
6. Y. Luo, *et al.*, Adaptive tactile interaction transfer via digitally embroidered smart gloves. *Nature Communications* **15** (1), 868 (2024).
7. J. Li, *et al.*, Thin, soft, 3D printing enabled crosstalk minimized triboelectric nanogenerator arrays for tactile sensing. *Fundamental Research* **3** (1), 111–117 (2023).
8. D. Kong, *et al.*, Super-resolution tactile sensor arrays with sparse units enabled by deep learning. *Science Advances* **11** (27), eadv2124 (2025).
9. J. Qi, F. Gao, G. Sun, J. C. Yeo, C. T. Lim, HaptGlove—untethered pneumatic glove for multimode haptic feedback in reality–virtuality continuum. *Advanced Science* **10** (25), 2301044 (2023).
10. M. Zhu, Z. Sun, C. Lee, Soft modular glove with multimodal sensing and augmented haptic feedback enabled by materials' multifunctionalities. *ACS nano* **16** (9), 14097–14110 (2022).
11. J. An, *et al.*, Fabric integrated wearable glove with a twisted string actuator for manual handling tasks. *Scientific Reports* **15** (1), 13185 (2025).
12. C. Pacchierotti, *et al.*, Wearable haptic systems for the fingertip and the hand: taxonomy, review, and perspectives. *IEEE Transactions on Haptics* **10** (4), 580–600 (2017).
13. S. Zhang, *et al.*, Artificial skin based on visuo-tactile sensing for 3D shape reconstruction: material, method, and evaluation. *Advanced Functional Materials* **35** (1), 2411686 (2025).
14. S. Li, *et al.*, When vision meets touch: A contemporary review for visuotactile sensors from the signal processing perspective. *IEEE Journal of Selected Topics in Signal Processing* **18** (3), 267–287 (2024).
15. S. Li, *et al.*, Biomimetic multimodal tactile sensing enables human-like robotic perception. *Nature Sensors* **1** (1), 52–62 (2026).
16. W. Yuan, S. Dong, E. H. Adelson, Gelsight: High-resolution robot tactile sensors for estimating geometry and force. *Sensors* **17** (12), 2762 (2017).
17. S. Li, *et al.*, AirTouch: A low-cost versatile visuotactile feedback system for enhanced robotic teleoperation, in *2025 IEEE/RSJ International Conference on Intelligent Robots and Systems (IROS)* (IEEE) (2025), pp. 15525–15532.
18. SenseGlove, SenseGlove Nova 2, https://www.senseglove.com/product/nova-2/ (2025), accessed: 3 May 2026.
19. K. Yao, *et al.*, Encoding of tactile information in hand via skin-integrated wireless haptic interface. *Nature Machine Intelligence* **4** (10), 893–903 (2022).
20. S. Kang, *et al.*, An 18-g haptic feedback ring with a three-axis force-sensing skin. *Nature Electronics* pp. 1–13 (2025).
21. C. du Pasquier, *et al.*, Haptiknit: Distributed stiffness knitting for wearable haptics. *Science Robotics* **9** (97), eado3887 (2024).

22. Z. Sun, M. Zhu, X. Shan, C. Lee, Augmented tactile-perception and haptic-feedback rings as human-machine interfaces aiming for immersive interactions. *Nature Communications* **13** (1), 5224 (2022).
23. H. Zhang, S. Hu, Z. Yuan, H. Xu, DOGlove: Dexterous manipulation with a low-cost open-source haptic force feedback glove, in Proceedings of Robotics: Science and Systems (LosAngeles, CA, USA) (2025), doi:10.15607/RSS.2025.XXI.104.
24. Y. Liu, et al., Electronic skin as wireless human-machine interfaces for robotic VR. Science Advances 8 (2), eabl6700 (2022).
25. J.-H. Youn, et al., Skin-attached haptic patch for versatile and augmented tactile interaction. Science Advances 11 (12), eadt4839 (2025).
26. M. Zhu, et al., Haptic-feedback smart glove as a creative human-machine interface (HMI) for virtual/augmented reality applications. Science Advances 6 (19), eaaz8693 (2020).
27. G. Xu, et al., Self-powered electrotactile textile haptic glove for enhanced human-machine interface. Science Advances 11 (12), eadt0318 (2025).
28. C. Yiu, et al., Skin-interfaced multimodal sensing and tactile feedback system as enhanced human-machine interface for closed-loop drone control. Science Advances 11 (13), eadt6041 (2025).
29. N. Vanichvoranun, H. Lee, S. Kim, S. H. Yoon, Estatig: Wearable haptic feedback with multiphalanx electrostatic brake for enhanced object perception in vr. Proceedings of the ACM on Interactive, Mobile, Wearable and Ubiquitous Technologies 8 (3), 1–29 (2024).
30. M. Park, et al., Stretchable glove for accurate and robust hand pose reconstruction based on comprehensive motion data. Nature Communications 15 (1), 5821 (2024).
31. W. Wang, et al., Neuromorphic sensorimotor loop embodied by monolithically integrated, low-voltage, soft e-skin. Science 380 (6646), 735–742 (2023).
32. C. Zhang, et al., VET: A visual-electronic tactile system for immersive human-machine interaction, in 2025 IEEE/RSJ International Conference on Intelligent Robots and Systems (IROS) (IEEE) (2025), pp. 21590–21595.
33. A. Tashakori, et al., Capturing complex hand movements and object interactions using machine learning-powered stretchable smart textile gloves. Nature Machine Intelligence 6 (1), 106–118 (2024).
34. Z. Tang, Y. Guo, C. Xiao, MFE: A multimodal hand exoskeleton with interactive force, pressure and thermo-haptic feedback. IEEE Robotics and Automation Letters (2026).
35. G. Pavlakos, et al., Reconstructing hands in 3d with transformers, in Proceedings of the IEEE/CVF Conference on Computer Vision and Pattern Recognition (CVPR) (2024), pp. 9826–9836.
36. K. Yao, et al., A fully integrated breathable haptic textile. Science Advances 10 (42), eadq9575 (2024).
37. Y. Tang, et al., Digital channel–enabled distributed force decoding via small datasets for hand-centric interactions. Science Advances 11 (4), eadt2641 (2025).

38. Z. Zhang, et al., Active mechanical haptics with high-fidelity perceptions for immersive virtual reality. Nature Machine Intelligence 5 (6), 643–655 (2023).
39. K. Goyal, D. A. Borkholder, S. W. Day, Dependence of skin-electrode contact impedance on material and skin hydration. Sensors 22 (21), 8510 (2022).
40. A. R. Moritz, F. Henriques Jr, Studies of thermal injury: II. The relative importance of time and surface temperature in the causation of cutaneous burns. The American journal of pathology 23 (5), 695 (1947).
41. S. Mak, et al., Use of massage therapy for pain, 2018-2023: a systematic review. JAMA Network Open 7 (7), e2422259 (2024).
42. T. Field, Massage therapy research review. Complementary Therapies in Clinical Practice 20 (4), 224–229 (2014).
43. B. R. Seo, et al., Skeletal muscle regeneration with robotic actuation-mediated clearance of neutrophils. Science Translational Medicine 13 (614), eabe8868 (2021), doi:10.1126/scitranslmed.abe8868.

Figures

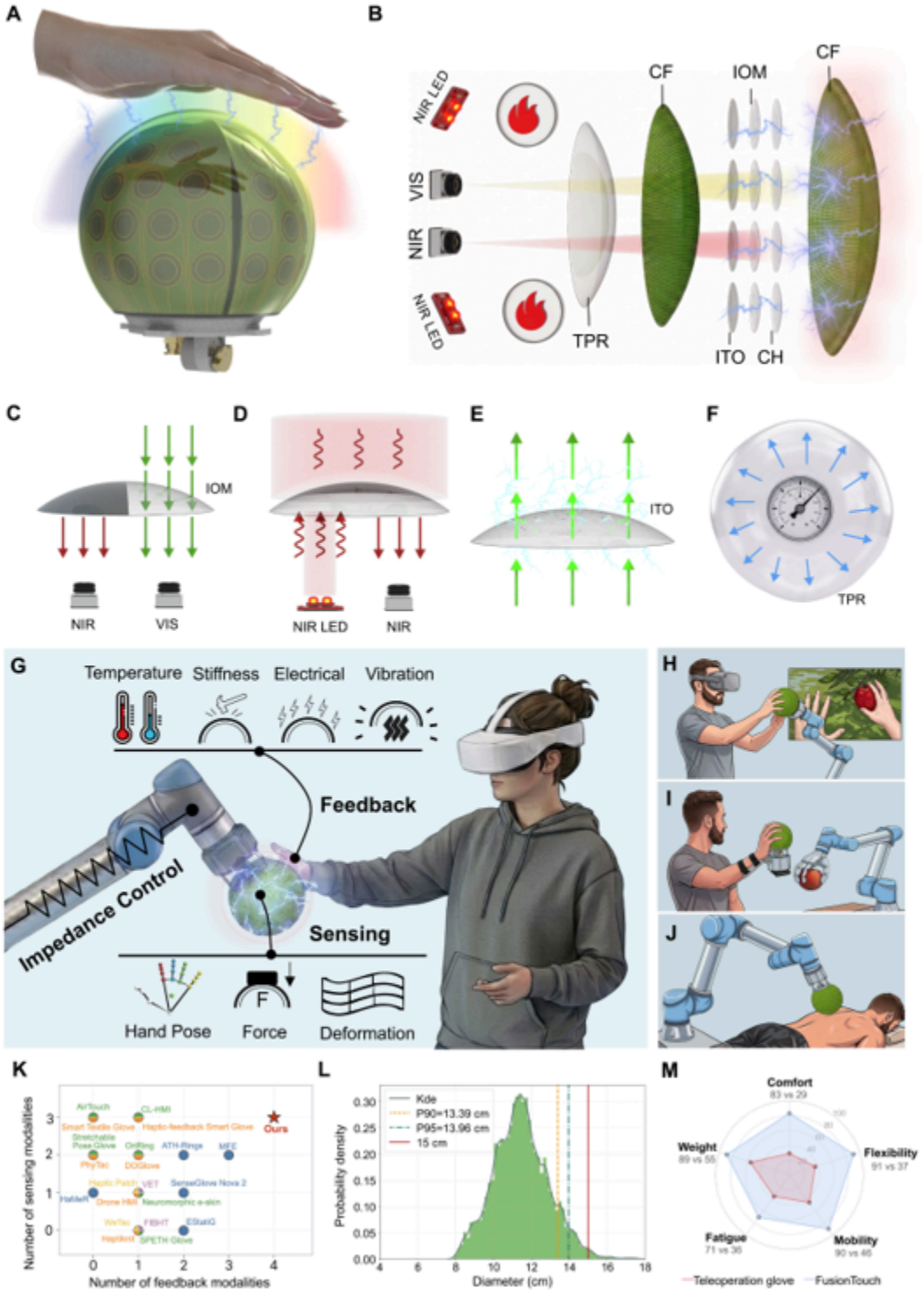


Figure 1

Structure, working principle and applications of FusionTouch. (**A**) FusionTouch perspective view. (**B**) Multispectral bidirectional skin consisting of chiffon fabric (CF), a thermoplastic rubber (TPR) support layer, infrared-opaque markers (IOMs), a transparent indium tin oxide (ITO) conductive layer, and conductive hydrogel (CH), while using visible light (VIS) and near-infrared (NIR) light from NIR light-emitting diodes (NIR LEDs) for spectrally separated sensing and feedback. (**C**–**F**) Key components of

FusionTouch: (**C**) Spectral separation layer, (**D**) NIR photothermal feedback path, (**E**) Transparent ITO electrotactile electrode, and (**F**) Pneumatic stiffness-modulation mechanism. (**G**) FusionTouch mounted on a robotic arm as a multimodal sensing and feedback interface. (**H**–**J**) Representative applications in virtual reality, teleoperation, and robot-assisted massage. (**K**) Performance comparison with state-of-the-art human-machine interfaces. (**L**) Gesture dataset collected from 20 volunteers. (**M**) Five-factor comparison between teleoperation gloves and FusionTouch.

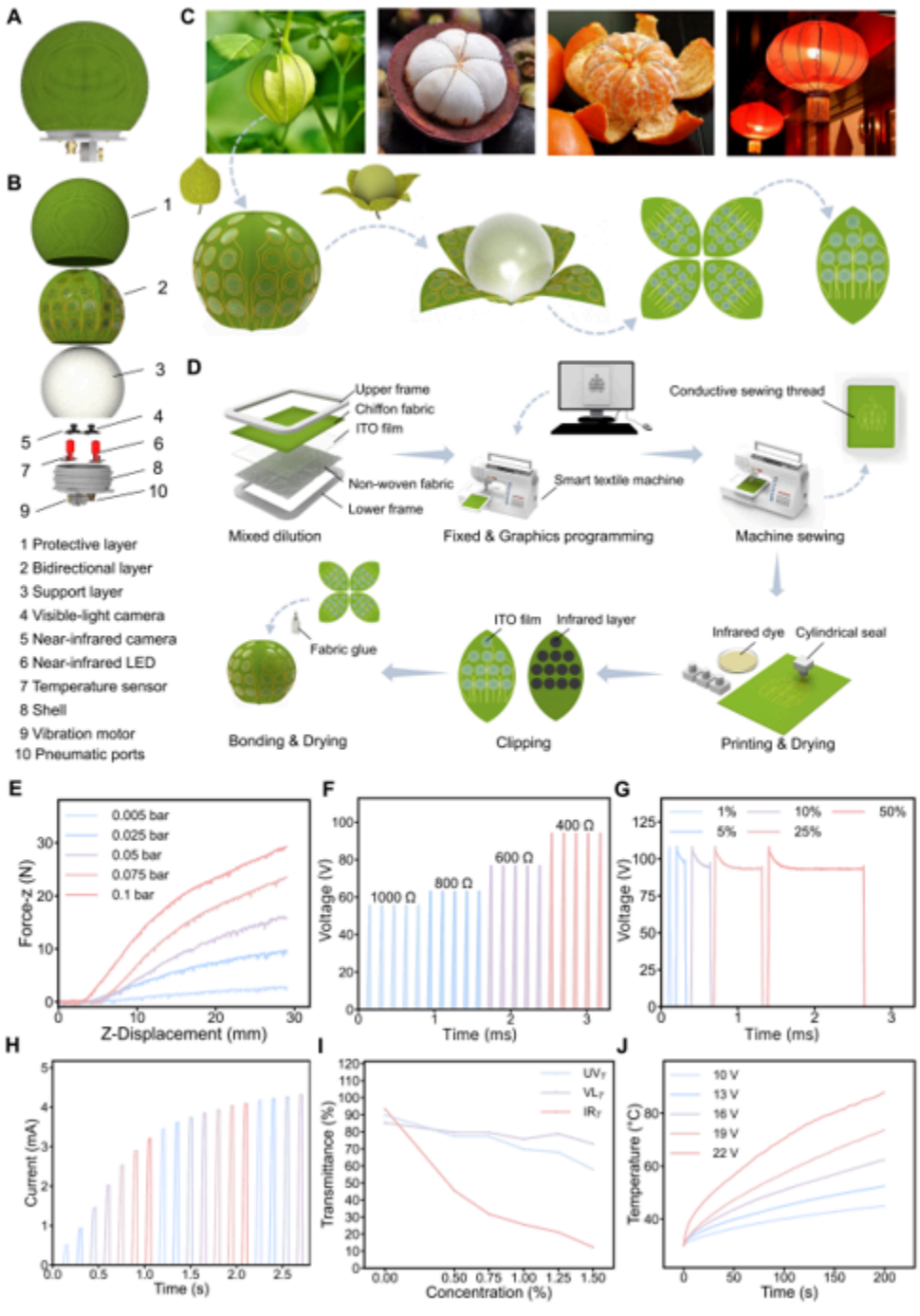


Figure 2

Fabrication and performance characterization of FusionTouch. (**A**) Rendering of FusionTouch. (**B**) Exploded view of FusionTouch. (**C**) Modular design inspired by natural multilayered structures, including lantern fruits, mangosteens, and oranges, enabling the transformation of a three-dimensional geometry into two-dimensional planar components. (**D**) Fabrication process of FusionTouch. (**E**) Force–displacement curves under different pneumatic pressures. (**F**) Output voltage curves under different resistances, demonstrating adjustable maximum voltage output. (**G**) Output voltage curves under different duty cycles, demonstrating tunable pulse width. (**H**) Adjustable current intensity controlled by the current-control module. (**I**) Spectral responses of optical coatings with different concentrations. (**J**) Surface temperature changes of FusionTouch induced by infrared LEDs under different driving voltages.

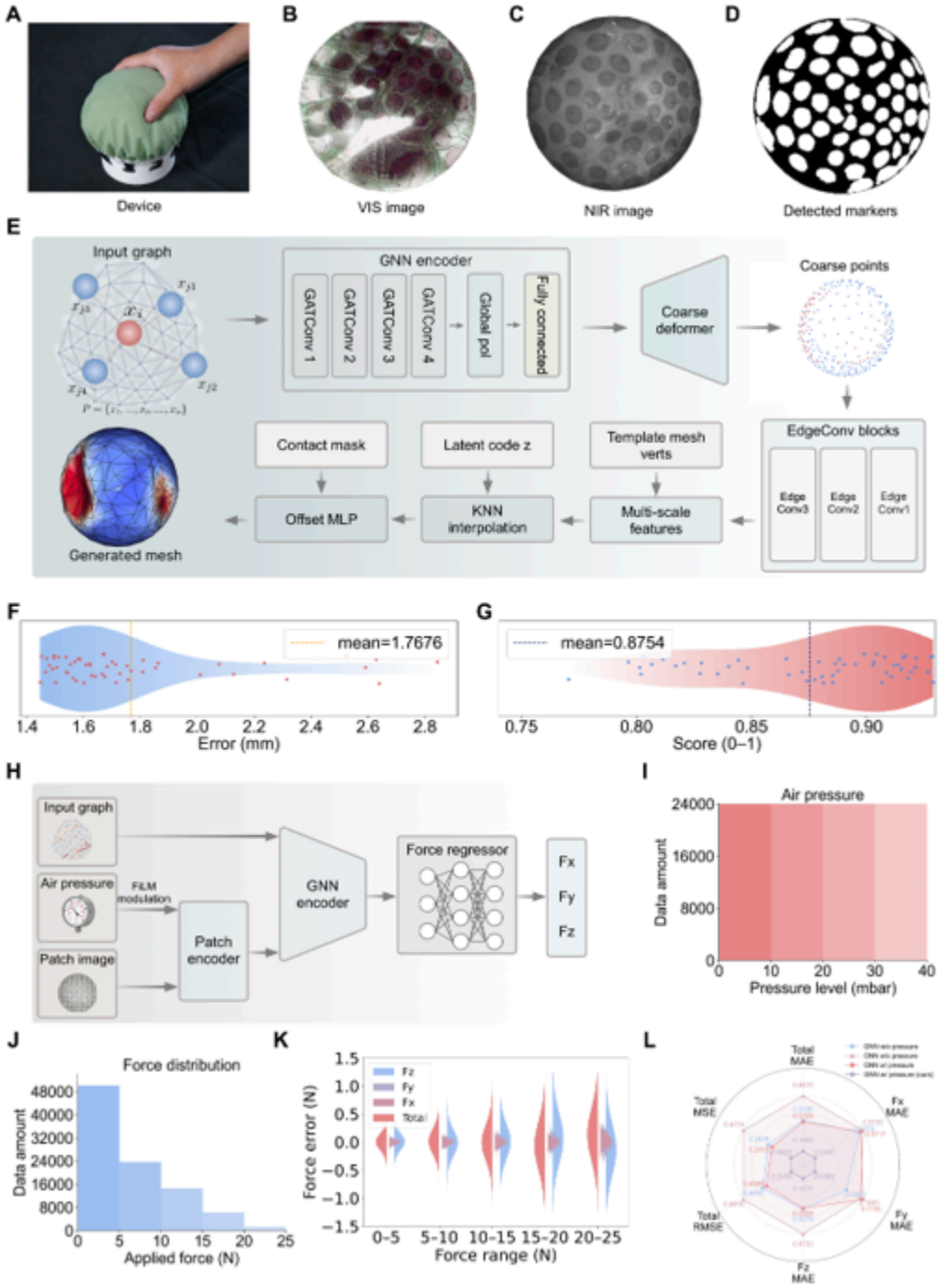


Figure 3

3D surface-deformation reconstruction and contact-force estimation. (**A**) Photograph of hand contact with FusionTouch. (**B**) Captured visible-light image. (**C**) Captured near-infrared image. (**D**) Marker segmentation from the near-infrared image. (**E**) 3D surface-deformation reconstruction pipeline. (**F**) Chamfer distance and RMSE distributions for reconstruction. (**G**) Reconstruction accuracy distribution based on ICP registration. (**H**) Force perception pipeline. (**I**) Air pressure distribution during contact-force perception experiments. (**J**) Force distribution during contact-force perception experiments. (**K**) Force perception accuracy distribution. (**L**) Prediction accuracy comparison among different force perception algorithms.

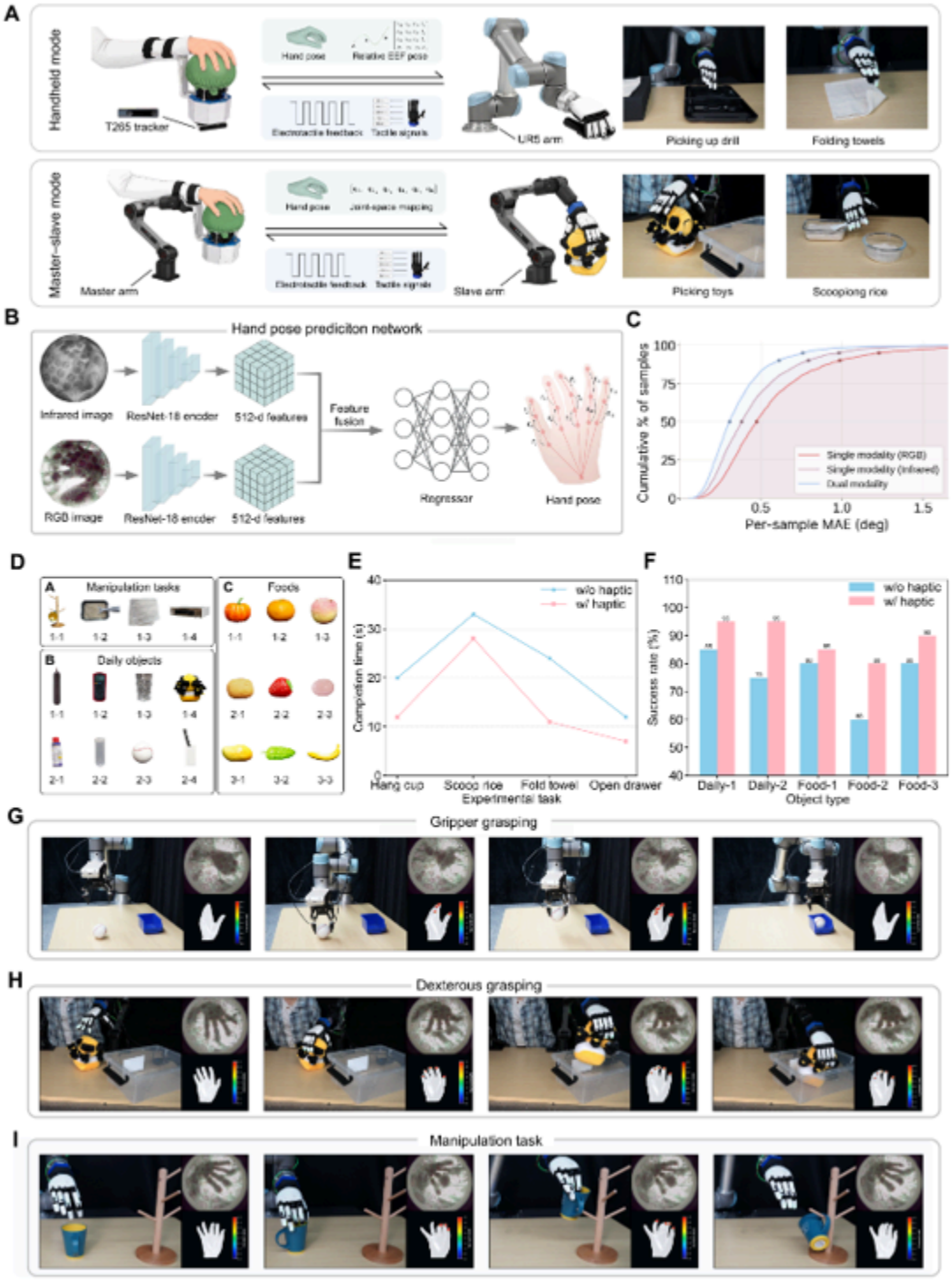


Figure 4

Hand-pose estimation and teleoperation experiments. (**A**) Two-mode teleoperation control frame-work. (**B**) Hand-pose estimation based on visible-light and near-infrared image fusion. (**C**) Hand-pose estimation accuracy under different sensing modalities. (**D**) Overview of grasping and manipulation experi-ments with different objects. (**E**) Task completion time with and without tactile feedback (w/o, without; w/, with). (**F**) Grasping success rate with and without tactile feedback. (**G**) Teleoperated

grasping with a parallel gripper. (**H**) Teleoperated grasping with a dexterous robotic hand. (**I**) Teleoperated manipulation task.

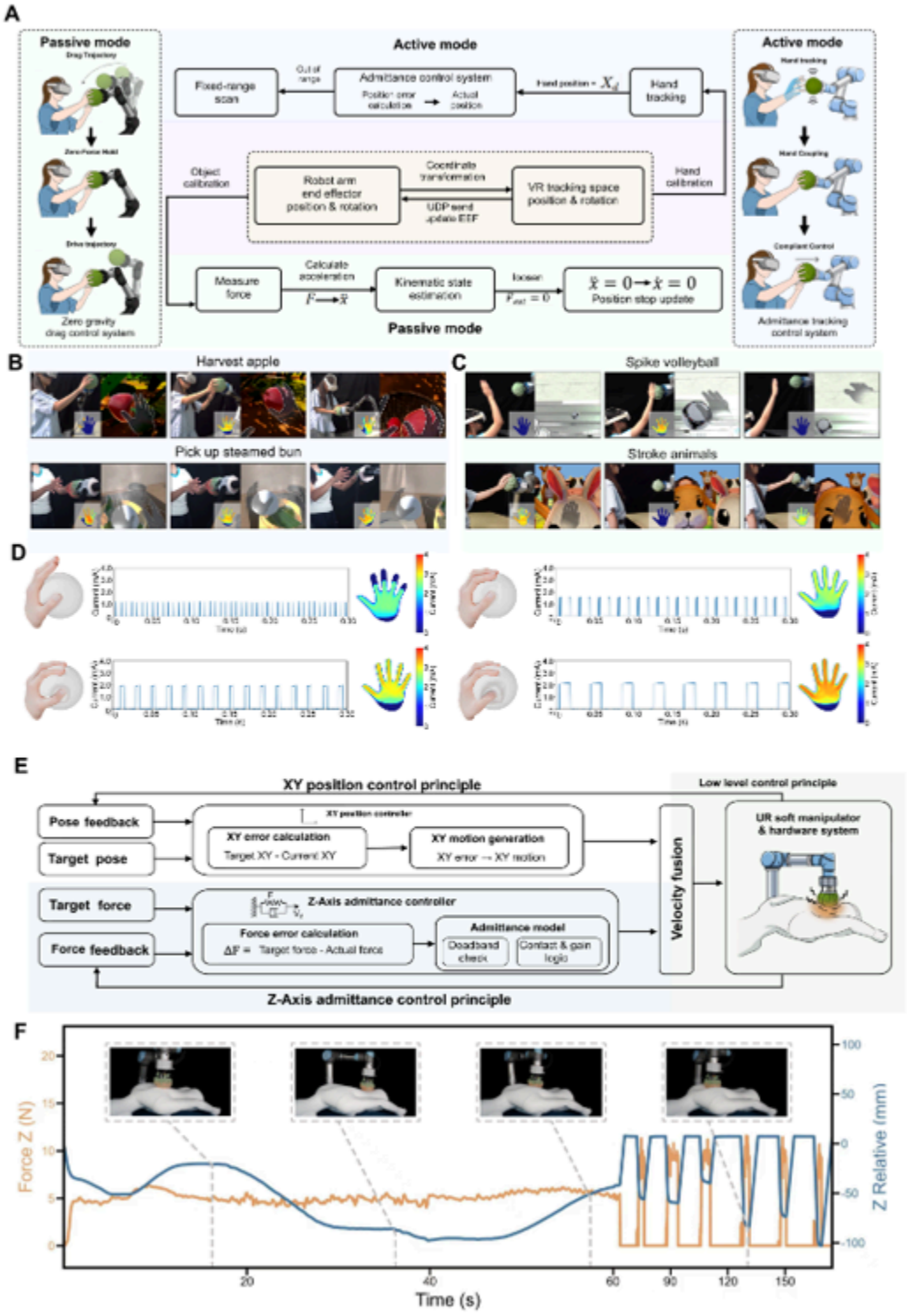


Figure 5

VR haptic interaction and robot-assisted massage demonstrations. (**A**) Robotic haptic feedback framework for virtual reality in active and passive modes. (**B**) Passive-mode application scenario. (**C**)

Active-mode application scenario. (**D**) Contact-dependent haptic feedback with different intensities. (**E**) Force-compliance control framework for robot-assisted massage. (**F**) Force and displacement curves during massage.

Supplementary Files

This is a list of supplementary files associated with this preprint. Click to download.

- MovieS2.Threedimensionalreconstructionbasedoninfraredmarkers.mp4
- SupplementaryDataS1.zip
- MovieS5.Teleoperatedmanipulationofhandheldtoolsandarticulatedobjects.mp4
- MovieS4.Teleoperatedgraspingoffragileanddailyobjects.mp4
- SupplementaryMaterial.pdf
- MovieS3.Teleoperatedmanipulationinfoldingandconstrainedplacementtasks.mp4
- MovieS7.Virtualrealitydynamicinteractiontasks.mp4
- MovieS6.Virtualrealityobjectpickupandmanipulationtasks.mp4
- MovieS1.OverviewofFusionTouch.mp4
- MovieS8.Massageexperimentsinsimulatedandrealhumancarescenariosx264.mp4